Applied Catalysis B: Environmental 228 (2018) 130–141

Contents lists available at ScienceDirect

Applied Catalysis B: Environmental

journal homepage: www.elsevier.com/locate/apcatb

Sn modification of TiO_2 anatase and rutile type phases: 2-Propanol photo-oxidation under UV and visible light

María Fernanda Gálvez-López[a], Mario J. Muñoz-Batista[b], Clemente Guadalupe Alvarado-Beltrán[a], Jorge Luis Almaral-Sánchez[a], Belén Bachiller-Baeza[b], Anna Kubacka[b,*], Marcos Fernández-García[b,*]

[a] Universidad Autónoma de Sinaloa, Fuente de Poseidón y Prol. Ángel Flores S/N, C.P. 81223 Los Mochis, Sinaloa, Mexico
[b] Instituto de Catálisis y Petroleoquímica, CSIC, C/Marie Curie, 2, 28049 Madrid, Spain

ARTICLE INFO

Keywords:
Anatase
Rutile
Doping
Quantum efficiency and yield
2-Propanol

ABSTRACT

In this work binary Sn-Ti samples having Sn:Ti atomic ratios from zero to one were prepared through a hydrothermal method. The resulting high surface area powders were characterized using a combination of X-ray diffraction, X-ray photoelectron spectroscopy, transmission electron microscopy, UV–vis spectroscopy and porosimetry techniques. The series of samples covers catalysts with anatase and rutile type structures. Each sample is composed of a main (anatase or rutile) $Ti_{1-x}Sn_xO_y$ phase decorated by different Sn-containing entities. The photo-catalytic performance in the 2-propanol photo-oxidation was assessed through the measurement of the reaction rate and true quantum efficiency. The latter required the measurement of the optical properties of the powders and the computation of the local superficial rate of photon absorption. Although relatively similar activity maximum can be obtained for anatase and rutite type samples based in the comparison of the reaction rates, the calculation of the true quantum efficiency demonstrates that the optimum anatase type material displays superior performance than the rutile one. The physico-chemical origin of this behavior is analyzed in terms of the electronic and structural properties of the binary Sn-Ti samples.

1. Introduction

Photo-catalysis is a technology used in liquid and gas phase chemical processes concerning the elimination of organic and inorganic pollutants, generation of high-added value organic compounds from raw or simple molecules (such as CO_2) or the production of new energy vectors such as hydrogen. Titania corresponds to the most utilized material in photocatalysis due to its inherent properties related to a modest cost, limited toxicity and outstanding chemical properties under illumination. However, the performance of bare titania materials can be improved by a number of strategies. Among them, the so-called doping of the titanium oxides was used almost from the beginning of the field [1–5].

Doping of titania has been extensively essayed using cations and/or anions as alien species to be introduced in the crystalline network of titania. Although with drawbacks, the best cases have been able to provide a better catalyst than the parent titania under UV but also under visible illumination. This is an important achievement required in order to obtain maximum profit from the sun and, therefore, for the fruitful use of such green energy source in modern photo-catalytic processes [1,2,5–11]. Among doping cations, Tin has been profusely tested in a number of photo-catalytic processes concerning the elimination of liquid phase pollutants such as phenol, cresol, or dyes [12–17], gas phase pollutants such as toluene, formaldehyde, acetone, or methyl-cyclohexene [18–22], or the photo-production of hydrogen from water or through reforming of bio-molecules [23–27]. The surface and bulk chemistry of Tin at titania oxides is so rich and complicate that it is difficult to be easily rationalized. From the works presented in the literature it appears that the (Tin) alien species tends to have an enriched surface concentration (compared with nominal one of the materials) and that it produces substitutional disordered mixed oxides with anatase or rutile structures, obviously occupying cation sublattice positions in both structures [13,14,16,22,28]. However, the exact synthesis conditions leading to pure anatase or rutile phases and how Tin is distributed (surface vs. bulk) within the catalytic solids are open questions. Moreover, depending of such structural properties as well as primary particle size and other (mostly unknown) morphological properties we can found that Tin incorporation at the titania-based solids has negligible effect in band gap energy [14], or triggers a relatively mild blue [18,29,30] or red [13,28,16] shift of such observable.

* Corresponding authors.
E-mail addresses: ak@icp.csic.es (A. Kubacka), mfg@icp.csic.es (M. Fernández-García).

https://doi.org/10.1016/j.apcatb.2018.01.075
Received 6 December 2017; Received in revised form 28 January 2018; Accepted 30 January 2018
Available online 31 January 2018
0926-3373/ © 2018 Elsevier B.V. All rights reserved.

The latter has obvious consequences in promoting or not the photo-activity of the systems under UV or, more importantly, sunlight illumination conditions.

In order to progress in the understanding of the Sn-Ti system, in this study we utilized a preparation method that can provide a series of samples with a relatively smooth transition from the anatase to the rutile polymorph as a function of the Tin content. Note that most of the studies carried out reported data using mixtures of anatase and rutile (and in some cases having additional minor contributions of other components, such as brookite or SnO_2 cassiterite) phases and this fact complicates the analysis of Sn structural and electronic effects on titania polymorphs. There are however some exceptions and literature reports on pure anatase and rutile Sn-Ti samples are available. Typically anatase is obtained for low doping concentration and moderate calcination temperatures while pure rutile is obtained after high temperature calcinations [24,28]. However, none of the above mentioned studies use the same preparation method to analyze in a single work both Sn-containing anatase and rutile based systems. This is carried out here using samples subjected to the same preparation procedure (including thermal treatment) and thus all having similar (high in our case) surface area, tendency of Sn to segregate at the surface from bulk positions of the titania structures, etc. In Sn-Ti binary systems, another important aspect concerns the effect of chlorine in the physico-chemical properties of the solids, as most of the studies used Tin (and in some cases Ti) precursors containing this anion [13–30].

Having thus a need for the understanding of Tin effects in the two more important titania photo-catalytic polymorphs, in this contribution we analyzed a large series of samples (10 solids) having Sn/Ti ratios from zero to one and having all high surface area, over 100 $m^2 g^{-1}$. These samples were characterized through a multitechnique approach using X-ray diffraction, porosimetry, transmission electron microscopy and X-ray photoelectron and UV–vis spectroscopies. Such a tool box was used to interpret the catalytic performance of the samples in the 2-propanol photo-oxidation under UV and sunlight-type illumination conditions. To provide a real measurement of the catalytic output, we calculated the true quantum efficiency of the reaction following recipes previously reported [31]. The results uncovers the complex structural situation taking place in both anatase and rutile type phases. This leads to different electronic effects and, consequently, to a rich situation concerning the influence of Tin in the catalytic activity of the titania polymorphs.

2. Experimental

2.1. Sample preparation

To carry out the synthesis of the Sn-Ti systems we prepare two solutions per sample. The first has titanium butoxide ($Ti(OBu)_4$; Sigma Aldrich) and nitric acid in ethanol (molar relation 2:30:2 for Ti:EtOH:HNO_3). The second includes tin dichloride ($SnCl_2$; Sigma Aldrich) and acetic acid in ethanol (molar relation 1:60:4 for Sn:EtOH:CH_3COOH). Both solutions were subjected to 30 min agitation. After it, the Sn-containing solution was introduced (in the quantity required for the desired Sn/Ti atomic ratio) in the other solution and the resulting solution agitated for other 30 min, and thus introduced into a 100 mL steel autoclave, internally covered with Teflon. The autoclave was introduced in a furnace at 200 °C during 6 h. The powders obtained were subsequently introduced in a Petri dish and dried at ambient temperature. Selected samples were repeatedly rinsed with distilled water until a test with silver nitrate did not detect chlorine ions at the solution.

2.2. Characterization of the samples

Ti and Sn content of the solids was measured with; (i) total reflection x-ray fluorescence (TRXF) using a Bruker – S2 PicoFox TXRF spectrometer, and (ii) atomic emission with inductive coupled plasma (ICP-AES) using a Optima 3300DV Perkin Elmer spectrometer. The BET surface areas and average pore sizes were measured by nitrogen physisorption (Micromeritics ASAP 2010). XRD profiles were obtained with a Seifert D-500 diffractometer using Ni-filtered Cu Kα radiation with a 0.02° step and fitted using the Von Dreele approach to the Le Bail method [32]; particle sizes and microstrain were measured with XRD using the Willianson-Hall formalism [33]. UV–vis diffuse-reflectance spectroscopy experiments were performed on a Shimadzu UV2100 apparatus using $BaSO_4$ or Teflon as a reference, and the results presented as the Kubelka-Munk transform [34]. Band gap analysis for an indirect/direct semiconductor was carried out following standard procedures; e.g. plotting $(hva)^n$ (n = ½ or 2 for indirect or direct semiconductor; hv = excitation energy, a = absorption coefficient, assumed to be proportional to the Kubelka-Munk transform in the relevant wavelength range) vs. energy and obtaining the corresponding intersection of the linear fit with the baseline [35].

Transmission electron microscopy (TEM) and X-ray energy dispersive (XEDS) spectra were recorded with a JEOL 2100F TEM/STEM microscope. XEDS-mapping analysis was performed in STEM mode with a probe size of ~1 nm using the INCA x-sight (Oxford Instruments) detector. Specimens were prepared by depositing particles of the samples to be investigated onto a copper grid supporting a perforated carbon film. Deposition was achieved by dipping the grid directly into the powder of the samples to avoid contact with any solvent.

XPS data were recorded on 4 × 4 mm^2 pellets, 0.5 mm thick, prepared by slightly pressing the powered materials which were outgassed in the prechamber of the instrument at room temperature up to a pressure < $2{\cdot}10^{-8}$ torr to remove chemisorbed water from their surfaces. The SPECS spectrometer main chamber, working at a pressure < 10^{-9} torr, was equipped with a PHOIBOS 150 multichannel hemispherical electron analyser with a dual X-ray source working with Ag Kα ($h\nu$ = 1486.2 eV) at 120 W, 20 mA using C *1s* as energy reference (284.6 eV). Surface chemical compositions were estimated from XP-spectra, by calculating the integral of each peak after subtraction of the "S-shaped" Shirley-type background. The calculation uses the appropriate experimental sensitivity factors and the CASAXPS (version 2.3.15) software.

2.3. Catalytic measurements and calculations

The activity of the samples for 2-propanol photo-oxidation was tested using a continuous flow annular photo-reactor (pyrex) schematically depicted in Fig. S1 of the Supporting information. The catalyst (ca. 0.4 mg cm^{-2}) was deposited onto the inner tube as a thin layer from a suspension in ethanol. The illumination was generated by four fluorescent lamps (UV, Philips TL 6 W/08-F6T5 BLB, 6 W; Sunlight, Sylvania F6WBLT-65; 6W) symmetrically positioned outside the reactor. The reacting mixture (100 mL min^{-1} and 20 vol % O_2/N_2) was prepared from pure N_2 and O_2. 2-Propanol concentration was 1400 ppm by vaporization of the organic compound. The N_2/O_2 mixture was used to transport the gas-phase products from the liquid-containing saturator to the mainstream and distilled water was injected using a syringe pump (to achieve 90% relatively humidity at the gas stream). The concentrations of the reactant was analyzed using an online gas chromatograph (Agilent GC 6890) equipped with HP-PLOT-Q/HP-Innowax columns (0.5/0.32 mm I.D. × 30 m) and thermal conductivity and flame ionization detectors. Reaction rates were evaluated under steady state conditions, typically achieved after ca. 3–4 h from the irradiation starting. No change in activity was detected for all samples within the next 18 h.

The formulation of the quantum efficiency requires the calculation of the ratio between the number of reactant molecules transformed and the number of photons absorbed by the catalyst [36–39].

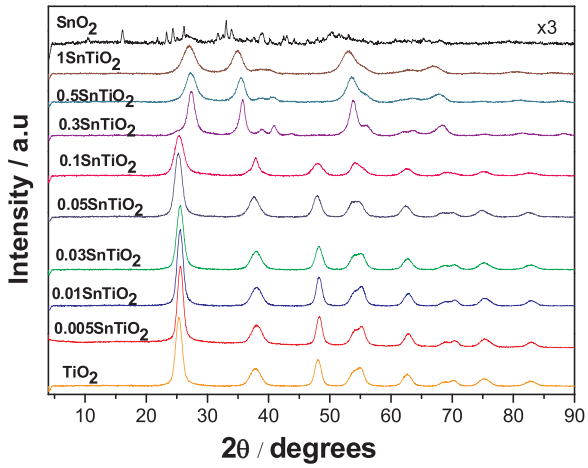

Fig. 1. XRD patterns of the samples.

$$\eta_q = \frac{\langle \text{reaction rate} \rangle \ (\text{mol m}^{-2}\text{s}^{-1})}{\langle \text{Photon Rate} \rangle \ (\text{Einstein m}^{-2}\text{s}^{-1})} \times 100 \quad (1)$$

The numerator of Eq. (1) is obtained from experimental catalytic experiments (described above). To evaluate the denominator of Eq. (1), we need to calculate the average superficial rate of photon absorption for the catalytic film used to evaluate the numerator (details described in the Supporting information file). This calculation takes into account the light-matter interaction in the reactor and considers all optical events (absorbance, transmittance, and reflectance) occurring in the catalyst-reactor system [31]. As input of such calculation, it is required to measure the optical properties (transmittance/absorbance and reflectance) of all components of the system as well as the lamp emission distribution function (corresponding data presented in Fig. S6).

3. Results and discussion

3.1. Physico-chemical properties

The XRD patterns of the samples are displayed in Fig. 1. The comparison with the TiO_2 reference indicates the dominant presence of the anatase phase (PDF 21-1272; space group $I4_1/amd$) for samples with a Tin:Titanium molar ratio below 0.1:1 ($0.1SnTiO_2$ sample). For the $0.1SnTiO_2$ sample the presence a broad bump immediately after the most intense (101) peak of the anatase (located at ca. 25.6°) indicates the incipient formation of the rutile phase (PDF 21-1276; space group $P4_2/mnm$). This last phase dominates the XRD patterns of the samples with higher Tin:Titanium ratios, although for the $0.3SnTiO_2$ specimen we can also observe the presence of a minor anatase contribution, pointed out by another bump at the left of the main (110) peak of the rutile phase (at ca. 27.4°). So, from XRD we can see that we obtain pure Sn-containing anatase and rutile phases, without appearance of other (brookite, cassiterite) crystallized phases, expect in two cases ($0.1SnTiO_2$ and $0.3SnTiO_2$ samples). The favoring of rutile crystallization in presence of Sn and thus its dominant presence for larger Tin contents have been previously observed in the literature [15,22,40]. For the two XRD-detected composite samples, the minor (anatase or rutile) phases do not display defined diffraction peaks, so we can not provide a reliable estimation of their weight contribution, being in any case relatively low. This is further discussed below.

The analysis of the primary crystallite size of the different anatase and rutile phases detected in the samples is presented in Table 1. The initial anatase phase has a decreasing size with the Sn content of samples, going from ca. 7 to about 5 nm. Similarly, the initial rutile phase appearing at the $0.3SnTiO_2$ sample has a primary crystallite size of ca. 6 nm and decreases significantly (up to ca. 3.5 nm) for the $1SnTiO_2$ sample. So, Tin produces a consistent decrease of primary particle size as its presence grows in both titania phases. Such a behavior has been previously observed [22,28,41]. In our case, this may be related to the relatively poor crystallization achieved by the SnO_2 cassiterite oxide (as shown in Figs. 1 and S7), indicating that the nucleation of Sn—O bonds is relatively difficult in the experimental conditions here used. Interestingly, the BET area of the Sn-Ti samples seems to correlate well with the primary crystallite size, displaying opposite trends (i.e. larger surface area for smaller primary crystallize size) along the sample series (Table 1). We also note that relatively similar BET surface areas are obtained for both titania polymorphs. Anatase surface area grows with Sn content from ca. 140 to 175 $m^2 g^{-1}$, while rutile does the same from ca. 145 to 165 $m^2 g^{-1}$. The correlation of the primary crystallite size and BET area (as well as other morphological parameters presented in Table 1) indicates that the porosity and, in general, morphology of the samples are relatively similar among them.

Table 1
Main physico-chemical properties of the samples.

Sample	Band gap (eV)		Anatase Size (nm)	Rutile Size (nm)	BET Area (m^2/g)	Pore volume (cm^3/g)	Pore size (nm)
	(hvF (R))^ (1/2)	(hvF (R)) ^2					
TiO_2	3.40		6.5	–	143.6	0.131	3.563
$0.005SnTiO_2$	3.26		7.4	–	139.1	0.097	2.808
$0.01SnTiO_2$	3.24		7.1	–	143.8	0.100	2.795
$0.03SnTiO_2$	3.24		6.1	–	161.2	0.119	2.973
$0.05SnTiO_2$	3.20		5.7	–	175.1	0.187	4.288
$0.1SnTiO_2$	3.12		5.1	–	165.9	0.153	3.695
$0.3SnTiO_2$		3.40		6.1	145.5	0.149	4.105
$0.5SnTiO_2$		3.42		4.1	155.9	0.168	4.320
$1SnTiO_2$		3.46		3.5	162.6	0.094	2.326
SnO_2		2.98	2.72[a]		1.35	0.0036	10.66

Average Standard Error: Band gap 0.03 eV; Size; 0.45 nm; BET area 3.5 m^2/g.
[a] Cassiterite phase.

The analysis of the XRD patterns also renders information about the cell parameters and volume (see Table S1 and Fig. 2). The ionic radius of Sn (0.69 Å) vs. Ti (0.605 Å) [42] indicates that, although both ions can be isoelectronic, the presence of Tin at bulk positions (in other words forming a mixed oxide) of titania phases must have structural effects. This is in fact what we can see in Fig. 2. Such figure displays values of the so-called tetragonallity parameter (a/c ratio) and cell volume along the samples (described in the figure by the Sn/Ti atomic ratio measured with TRXF and ICP-AES). In accordance with the ionic radius differences between Sn and Ti, we observed an increase of the cell volume along with the Sn content of the samples for both anatase and rutile phase phases. This increase is relatively mild until the Sn/Ti ratio is about 0.03 and grows afterwards. In the region where the anatase to rutile transformation takes place we observe a singular value which may be related to a specific situation of Sn (explored afterwards with other techniques). In the case of rutile the cell volume has a more drastic response due (at least in first approximation) to the larger Sn concentration of the samples. The tetragonallity ratio trend along the series shows however relative differences between the anatase and rutile phases. In anatase we found a more or less constant ratio (although with a rather modest decreasing tendency) indicating that both a and c parameters module (values reported in Table S1) increase is roughly similar, with no preferential release of the stress in any specific cell direction. In the case of rutile we found a decrease of the tetragonallity ratio, indicating a larger increase of the c vs. a parameter. Such a behavior has been previously observed in titania polymorphs as an effect of the presence of voluminous (ionic radius larger than Ti) alien species at substitutional positions of the networks [43,44]. In brief, the analysis of the XRD derived cell parameters and volume points out the presence of Tin at substitutional positions of all anatase and rutile phases

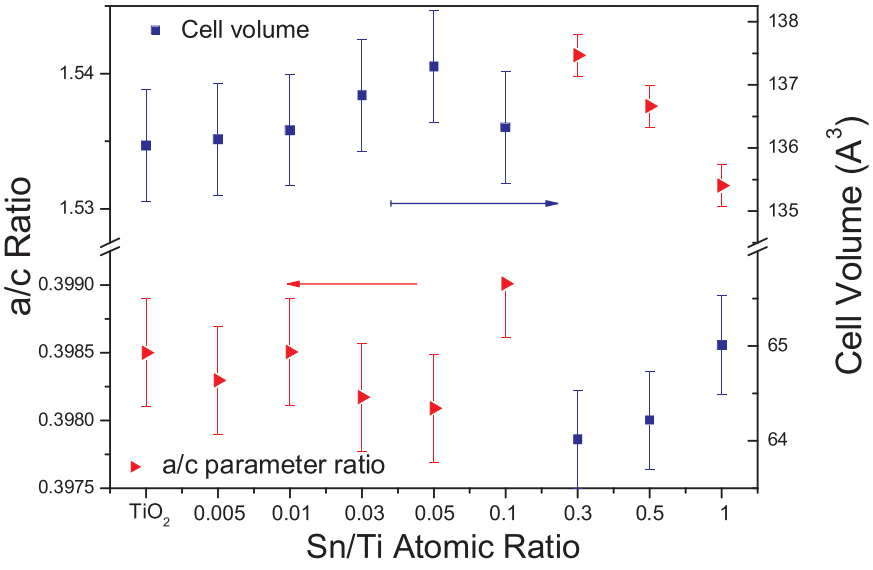

Fig. 2. Ratio between a and c cell parameters and cell volume vs. the Sn/Ti atomic ratio (obtained by TRXF) for the samples.

detected in our samples.

The structural and morphological characteristics of the samples were further analyzed using microscopy. Both general and detail views of selected samples are presented in the TEM micrographs included in Fig. 3. In the general views (panels a, c, e, and g of Fig. 3) we can see the agglomeration of individual crystallites which are well below 10 nm according to the more detailed views for all samples (panels b, d, f, and h). The crystallites correspond to the anatase phase for the $0.01SnTiO_2$ and $0.05SnTiO_2$ samples (see Fourier Transform displayed at the inset in panels b and d), with typical size around 5–7 nm, in broad agreement with XRD results. For the $0.1SnTiO_2$ we can observe a lower degree of crystallization and the Fourier transform of the image (inset in panel f) indicates the presence of both anatase and rutile phases. Individual particles are more complicated to be neatly observed in this sample. Similarly, the $0.3SnTiO_2$ sample appears poorly crystallized (in accordance with XRD analysis; Table 1) but in this case the electron diffraction indicates the dominant presence of the rutile phase, with no detection of anatase. The detailed view (panel h) has an arrow indicating that over the rutile crystallites we found a nearly amorphous overlayer, suggesting the presence of poorly crystallized entities which could be associated with Tin located at the surface of the dominant rutile phase. Microscopy was finally utilized to provide STEM mapping of the Tin and Titanium distribution within the solids. The corresponding STEM and mapping figures for Sn and Ti are collected in Fig. 4. From these figures we can see than Tin is homogenously distributed in the samples, no matter the anatase and rutile dominance in the structural composition.

To substantiate the presence of Tin at the surface of the materials as suggested by TEM as well as to analyze the oxidation state of the cations we carried out an XPS study of the samples. Such technique was also utilized to measure the Cl content of the solids. Thus, O 1s, Cl 2p, Ti 2p, and Sn 3d peaks were analyzed and results presented in Fig. 5. Peaks position after fitting are collected in Table 2 while some representative examples of the fitting procedure are presented in Fig. S8 of the Supporting information section. A first point to note is that all peaks measured has constant energy positions when anatase is the dominant structure (up to the $0.1SnTiO_2$ sample) and suffer an important shift to higher energies when rutile is the dominant phase (Table 2). The shift has a similar magnitude for all O 1s, Cl 2p, Ti 2p, and Sn 3d peaks, up to 0.6–0.8 eV for the $1SnTiO_2$ sample with respect to titania. This behavior has been observed previously in several experimental studies concerning Sn-Ti binary catalysts [13,28]. The synchronous shift in all atom constituents of the solids provides conclusive evidence of a decrease of the Fermi edge of the samples, taking place exclusively for rutile samples. This shift increases with the Tin content (within the rutile dominated samples) and would thus indicate that there is close contact between the rutile phase and the XRD-silent, surface Sn-containing phase detected by microscopy. The presence of a Sn-rich surface layer is however observed for all samples. In Fig. 6 (upper panel) we plot the Sn/Ti atomic ratio obtained from XPS against the same observable but obtained using TRXF and ICP-AES. For all samples we can observed a similar tendency, with a roughly linear correlation (slope ca. 1.9). Thus, although Sn has a tendency to be at the surface of all catalysts, only in the case of rutile this fact has an effect on the Fermi edge (triggered by phase contact with the minor, amorphous SnOx overlayer supported onto the dominant rutile phase). This can be justified according to the theoretical analysis of the SnO_2-TiO_2 interface [45]. Such analysis indicates that the electronic states of the Sn-containing entities interact efficiently with the bottom part of the conduction band of rutile while are relatively above in the anatase case. This clearly shows that the deposition of Sn-containing entities leads to strongly different electronic effects in anatase than rutile type materials. Also, that Fermi Edge effects in rutile are directly proportional to the Sn content by an increasing of the extent of the interaction.

The XPS study was also able to show that Sn and Ti showed a single oxidation state throughout all the sample series (Fig. S8; Table 2). If we discount the above mentioned Fermi edge shift, for all samples we observe "formal" binding energies of 485.95 ± 0.1 and 458.3 ± 0.1 eV, characteristic of the Sn(IV) and Ti(IV) oxidation states [46]. So, contributions of other oxidation states can be dismissed on the basis of the XPS analysis (see Fig. S8). XPS was also able to provide information about the chloride ions present at the samples. Chloride is introduced with Tin in the sample composition. The bottom panel of Fig. 6 plots the Cl/M (being M Tin and/or Titanium) ratio vs. the Sn/Ti ratio (obtained by TRXF and ICP-AES analysis) of the materials. Although Cl comes from the Sn precursor, the Cl/Sn and Cl/(Sn + Ti) plots indicate the existence of a saturation level in the amount of Cl taken by the material, which appears to be connected with the dominance of the rutile phase. Equally interesting is the fact that a roughly linear behavior is observed for the Cl/Ti ratio with respect to the bulk Sn/Ti ratio, indicating that Cl is mostly associated with the surface Ti component. The joint considering of the above mentioned facts would indicate that Chlorine is associated with surface titania no matter the structure but the presence of a Sn-containing overlayer (more extended over rutile type samples) limits the Cl uptake of the materials.

The characterization of the materials was completed with the measurement of the UV–vis spectra of the samples. The spectra of the TiO_2 and SnO_2 references are displayed together with the $xSnTiO_2$

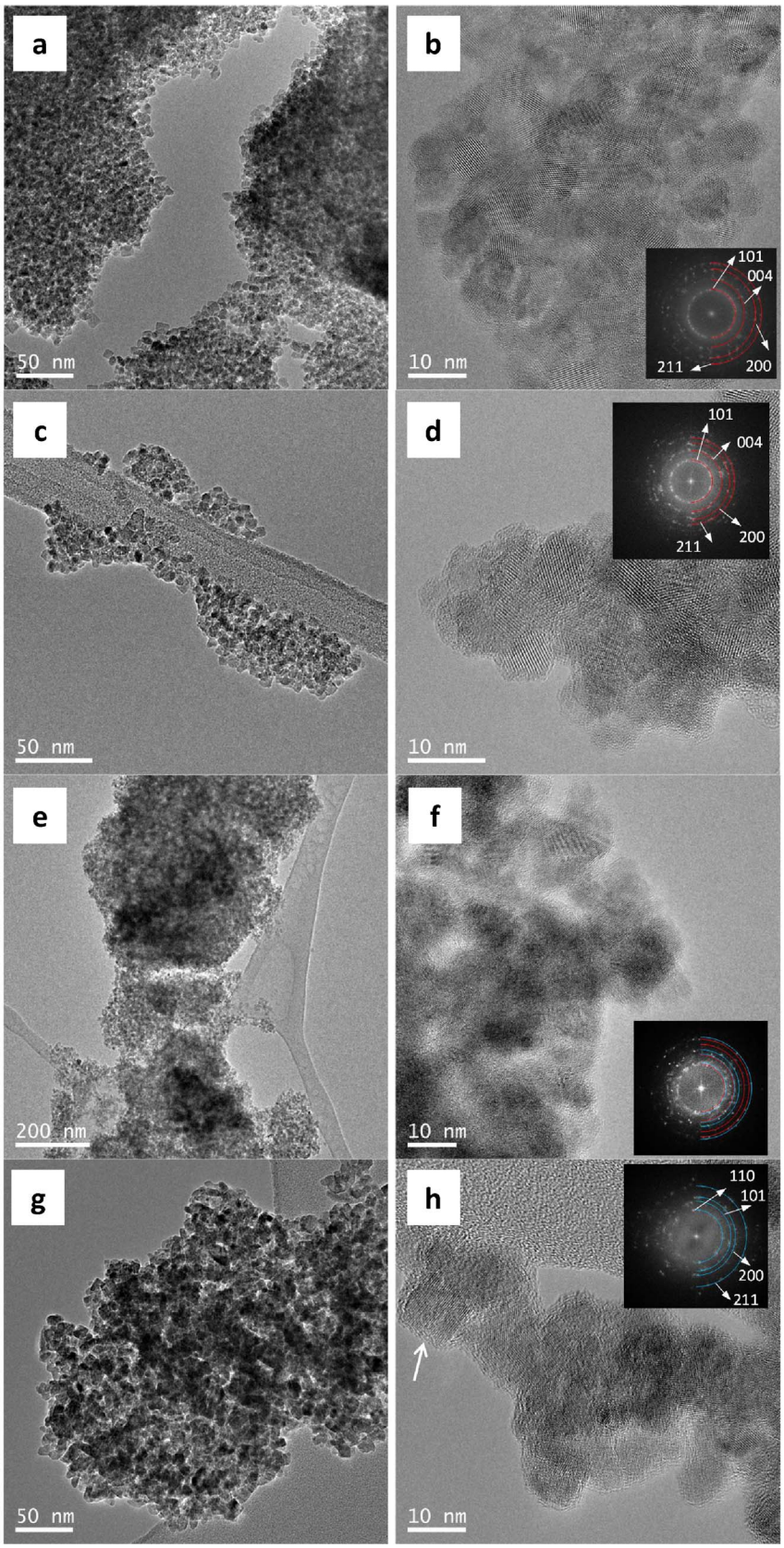

Fig. 3. TEM images and Fourier Transform (FT) patterns for the (a,b) 0.01$SnTiO_2$, (c,d) 0.05$SnTiO_2$, (e,f) 0.1$SnTiO_2$, and (g,h) 0.3$SnTiO_2$ samples.

samples in Fig. 7. The anatase TiO_2 reference shows absorption in the UV region while our poorly crystallized SnO_2 sample expands absorption into the visible region. TiO_2 anatase is an indirect gap semiconductor while rutile is a direct gap and SnO_2 cassiterite corresponds to a direct although forbidden gap semiconductor [35]. Our measurement of the band gap energy renders a value of 3.4 eV for the TiO_2 anatase and ca. 3 eV for SnO_2 cassiterite (Table 1). The corresponding measurements of the x$SnTiO_2$ samples evidence a progressive decrease

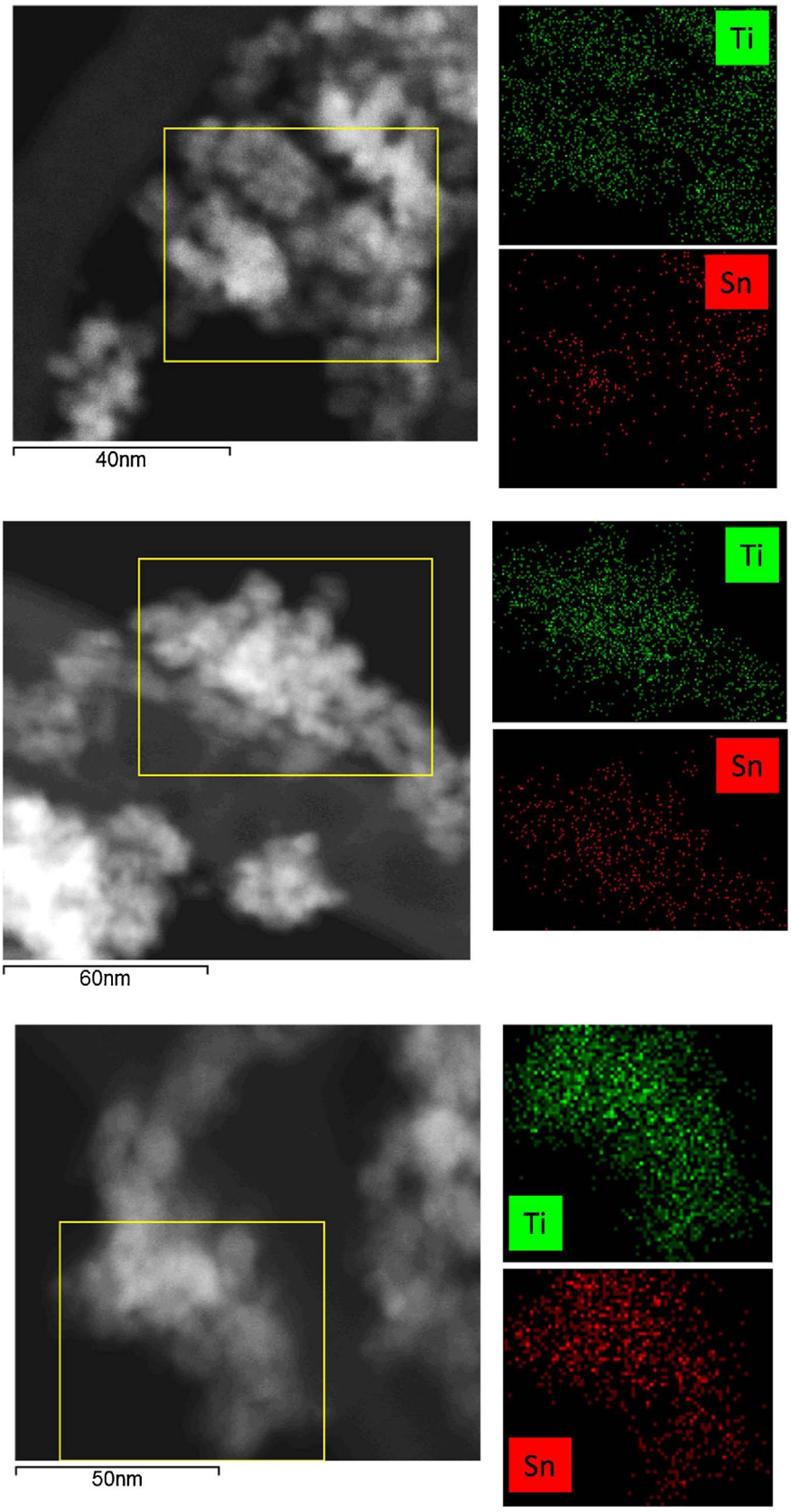

Fig. 4. STEM-mapping analysis of the $0.05SnTiO_2$ (top), $0.1SnTiO_2$ (middle), and $0.3SnTiO_2$ (bottom) samples.

of the (indirect-type) band gap energy with the Sn content of the samples in the anatase-based samples. This amounts for a relatively modest magnitude, ca. 0.3 eV. For rutile (direct-type), we observe a near constant value of 3.43 ± 0.03 eV for all samples. Of course, in the latter samples the interpretation is rather difficult as we have shown the existence of two phases, the rutile-TiO_2 and the XRD-silent SnO_x. The band gap obtained would thus be a weighted (by their molar percentage and optical cross section) average between both components. Although

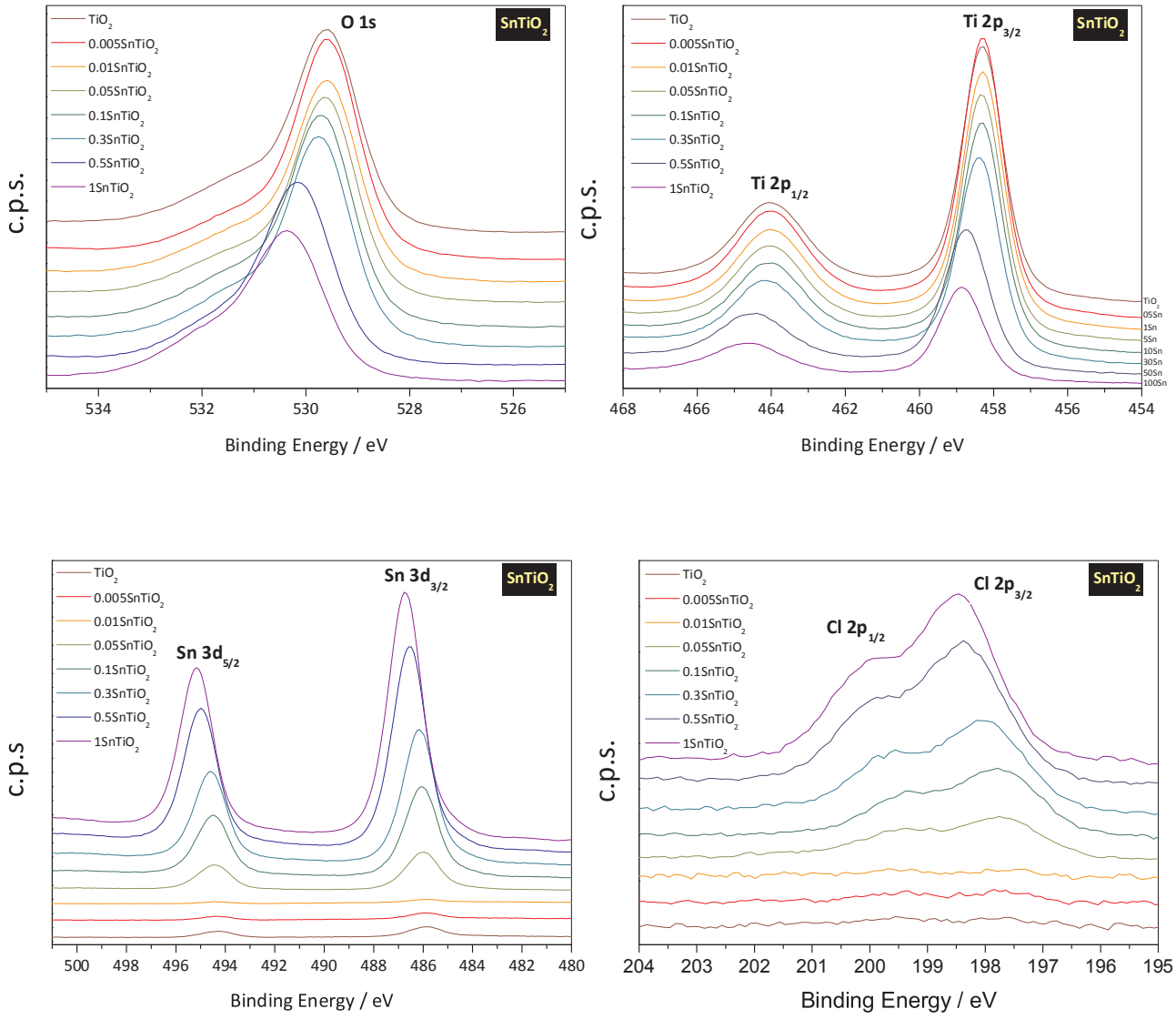

Fig. 5. XPS data for the samples.

we roughly known the molar percentage, we can not measure the optical properties of the amorphous overlayer and thus can not provide a more insightful analysis of this point.

So, the characterization study indicates the complexity of the resulting catalysts when Sn is progressively in contact with Ti. XPS found a nearly constant 2:1 ratio between Sn at the surface/subsurface positions with respect to bulk positions of the crystallites. On the other hand, the existence of $Ti_{1-x}Sn_xO_2$ phases is supported by the XRD analysis of cell parameters and volume as well as by the STEM-mapping showing an homogenous distribution of Sn at the samples. The joint consideration of these facts means that anatase or rutile phases are in fact substitutional mixed oxides ($Ti_{1-x}Sn_xO_2$) but with a Sn content of roughly 1/3 of the nominal one. At low Sn content we observe anatase structures with surface-enriched Sn zones, as depicted in Scheme 1. For samples having a 0.1:1 Sn:Ti ratio we start to see the nucleation of the rutile phase, which becomes dominant for ratios equal or above 0.3. Although the Sn enrichment of the surface is similar to the anatase case, the larger surface area covered by tin species as well as the known larger interaction with the rutile conduction band [45] triggers a change on the Fermi edge as well as the valence and conduction bands

Table 2
XPS binding energies (eV) and atomic ratios for the samples.

Sample	O 1s	Sn $3d_{5/2}$	Ti $2p_{3/2}$	Cl $2p_{3/2}$	Sn/Ti	O/(Sn + Ti)	Cl/Sn	Cl/Ti	Cl/Sn + Ti
TiO_2	529.6	485.9	458.3	197.7	0.007	2.82	–	–	–
$0.005SnTiO_2$	529.6	486.0	458.3	197.6	0.014	2.80	0.923	0.013	0.012
$0.01SnTiO_2$	529.6	486.0	458.3	197.6	0.027	2.75	0.565	0.016	0.015
$0.05SnTiO_2$	529.6	486.0	458.3	197.7	0.118	2.70	0.351	0.041	0.037
$0.1SnTiO_2$	529.7	486.0	458.3	197.7	0.294	2.64	0.211	0.062	0.048
$0.3SnTiO_2$	529.7	486.1	458.4	197.9	0.471	2.52	0.191	0.090	0.061
$0.5SnTiO_2$	530.1	486.5	458.7	198.3	1.041	2.22	0.175	0.182	0.089
$1SnTiO_2$	530.3	486.7	458.85	198.4	1.880	2.15	0.169	0.319	0.111

Average Standard Error: 0.01 eV (B.E.); 6.7% (atomic ratios).

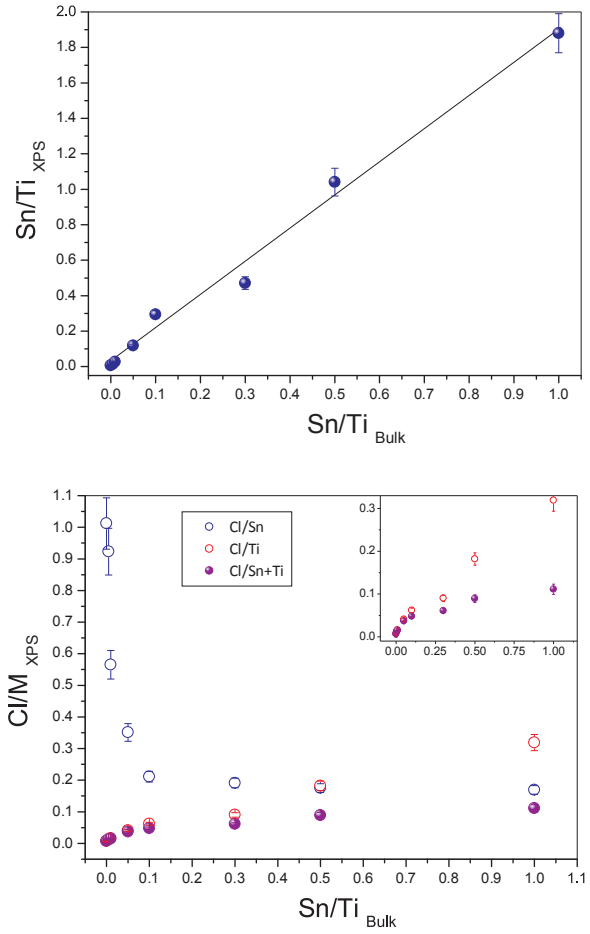

Fig. 6. Sn/Ti and Cl/M (M = metal) XPS atomic ratio vs. the Sn/Ti atomic ratio obtained from TRXF Analysis. A line with slope of 1.9 is displayed in the top panel.

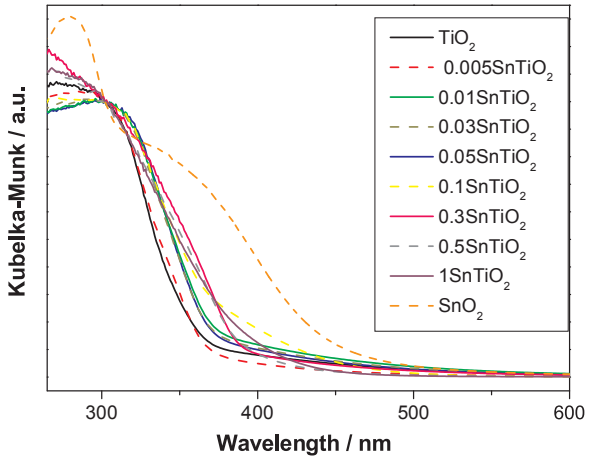

Fig. 7. UV–vis spectra of the samples.

of the composite system (see Scheme 1). Note also that considering the large band gap energy of the amorphous Sn-containing surface phase (should be larger than the ca. 3.0 eV-detected for our cassiterite reference- by confinement effects, see Ref. [35]) we expect that holes produced in such phase would be driven to the rutile one. However, the lack of information about the exact band gap of such extended surface entities and thus the position of the valence band (and its potential variation with the Sn:Ti ratio, occurring exclusively within rutile type samples) only allow to plot a block (assuming the band position from ca. 3 to 3.5 eV) representing an undefined position the valence band in

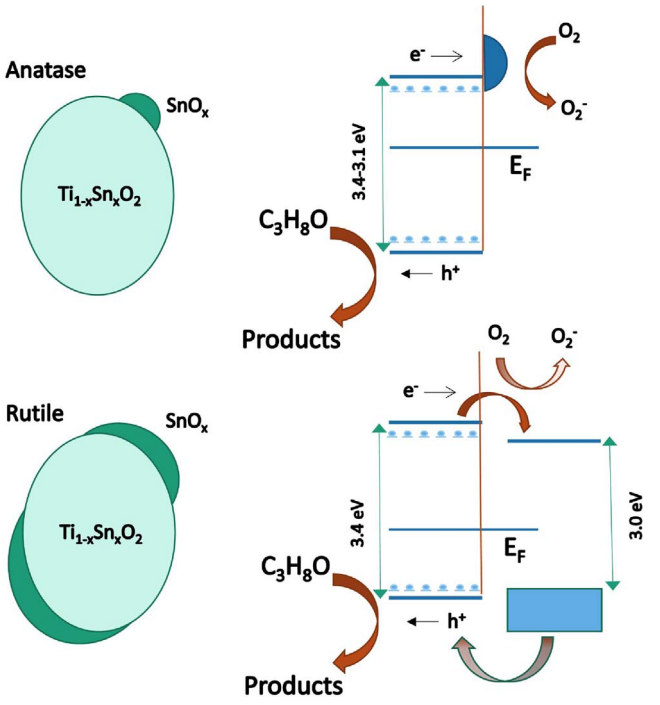

Scheme 1. Left: representation of the existent entities/phases present in the binary Sn-Ti system with anatase and rutile-type structures. Right: simplified diagrams showing most important electronic and chemical processes taking place under illumination. Degraded color arrows indicate processes taking place or not or varying as a function of the Sn content of the solid. See text for details.

Scheme 1. Still such representation is enough to understand charge handling through interfaces in the composite system. In Section 3.2 we discussed the charge handling and chemical consequences of the electronic effects associated with the structural and electronic properties of the composite materials as a function of the Sn:Ti atomic ratio of the samples. In all samples, irrespective of the anatase or rutile structure we detected the presence of chlorine at the surface of the materials in close interaction with surface Ti sites.

3.2. Catalytic properties

As mentioned in the introduction this work attempts to measure the photo-activity of anatase and rutile type based samples for high surface area Sn-Ti samples. To this end we have measured the gas-phase elimination of 2-propanol. 2-propanol is a volatile organic pollutant presents at urban atmospheres and particularly at indoor environments. Among the most typical sources of this pollutant, we can enumerate construction materials, household products, waxes, varnishes and many others [47–50]. Therefore this pollutant can be considered a classical benchmark for gas-phase photo-oxidation processes, explored in numerous publications [50–53].

In order to provide a real, quantitative assessment of the catalytic performance, we followed the IUPAC advice and calculate the quantum efficiency of the catalysts. To do it, we first measured the local superficial rate of photon absorption (details of the optical measurements and computational procedures are presented at the Supporting information section). Figs. 8 and 9 provide plots for this observable obtained under UV and sunlight-type illumination, respectively. The panels show the value of such observable along the surface of the catalytic film at the reactor (see Fig. S1 for a schematic view of the reactor) and identifies differences among the samples. Larger values of the local superficial rate of photon absorption are observed as the Tin content of the materials grows, irrespectively of the illumination source.

The evaluation of the catalytic properties of the solids was thus carried out using first the reaction rate and second the true quantum

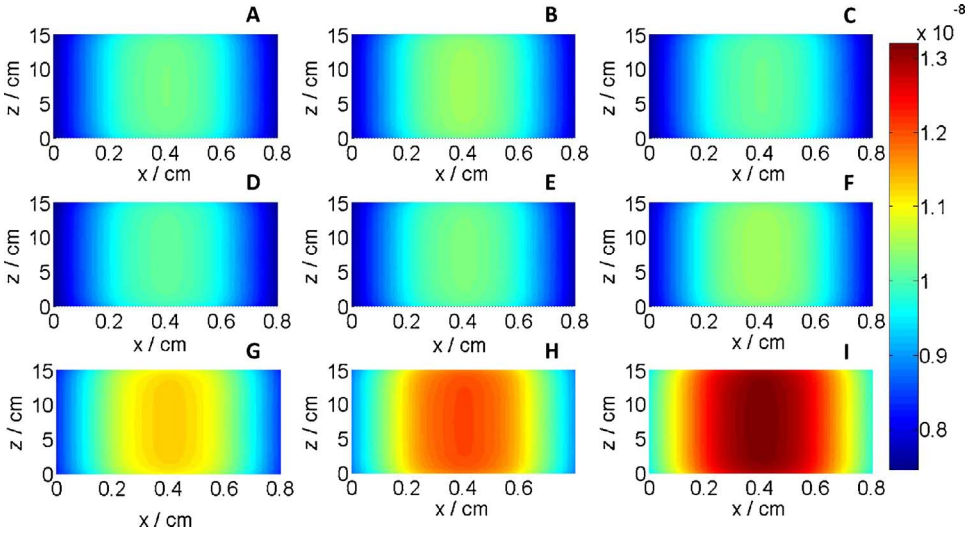

Fig. 8. Local superficial rate of photon absorption (Einstein $cm^{-2} s^{-1}$) of the samples under UV illumination. (A) TiO_2, (B) $0.005SnTiO_2$, (C) $0.01SnTiO_2$, (D) $0.03SnTiO_2$, (E) $0.05SnTiO_2$, (F) $0.1SnTiO_2$, (G) $0.3SnTiO_2$, (H) $0.5SnTiO_2$, (I) $1SnTiO_2$.

efficiency. Values for these observables are collected in Fig. 10 for UV and sunlight-type illumination. The important differences (larger than a factor of 6) observed under UV and sunlight-type illumination for all samples indicate the importance of UV photons in the catalytic performance achieved upon sunlight-type illumination. Still, we note that our nano-titania and Sn-Ti samples show some activity for visible photons, as described earlier for (defective) nanostructured titania and in contraposition to P25 and other samples with large primary particle size and anatase or rutile structure [2,4].

Under both illumination conditions we encountered two local activity maxima. Considering the reaction rate, relatively similar (although favoring the rutile type sample under UV) values for the $0.01SnTiO_2$ and $0.3SnTiO_2$ samples are observed, irrespective of the illumination conditions (Fig. 10). Considering the true quantum efficiency, the relative performance of these two samples varies. Differences in optical properties of the solids (Figs. 8 and 9) drive to a different result under UV or sunlight-type illumination. Table 3 facilitates the quantitative comparison between the local maxima. As mentioned, reaction rates values are relatively close although favoring the rutile-type catalyst under UV and equal within error under sunlight-type illumination. Considering the efficiency, under UV we observe similar values (ratio 0.84; Table 3) but under sunlight-type illumination the anatase-type system ($0.01SnTiO_2$) overperforms the rutile-type system by ca.130% (factor ca. 2.3; Table 3).

We can attempt to compare the reaction rate and maximum quantum efficiency here achieved using the optimum sample, $0.01SnTiO_2$, with previously reported values. For gas-phase 2-propanol photo-oxidation, previous studies using composite Sn-Ti samples obtained by deposition of SnO_x species onto Degussa P25 render optimum values for ca. 1 mol. % of SnO_2 under UV–vis illumination but displayed limited reaction rates [54]. A somewhat similar, relatively limited catalytic performance was reported for the chemically-similar acetone molecule using binary Sn-Ti systems [18]. Both works used batch (and not continuous as here) reactors making difficult to extract reasonable conclusions in relation to the comparison with our binary Sn-Ti samples. Comparison of true quantum efficiency can be carried out with Degussa P25 but also with other titania samples having anatase-rutile composition [55]. We did not found any previous measurement of the true quantum efficiency using binary Sn-Ti systems. In spite of it, optimum values under UV or sunlight-type illumination conditions are reported for optimized anatase-rutile samples having ca. 10 mol. % of rutile. Such sample has ca. 10% lower activity under UV but ca. 10 times larger under sunlight-type conditions. P25 displays a UV value near 3 times lower than the $0.01SnTiO_2$ sample and almost negligible activity under sunlight-type conditions. Therefore, the comparisons available at the literature indicate the important activity reached with the $0.01SnTiO_2$ sample under all illumination conditions here tested but particularly under UV.

The complex structural and electronic properties of the solids make the physical interpretation of the activity rather complex. We observed

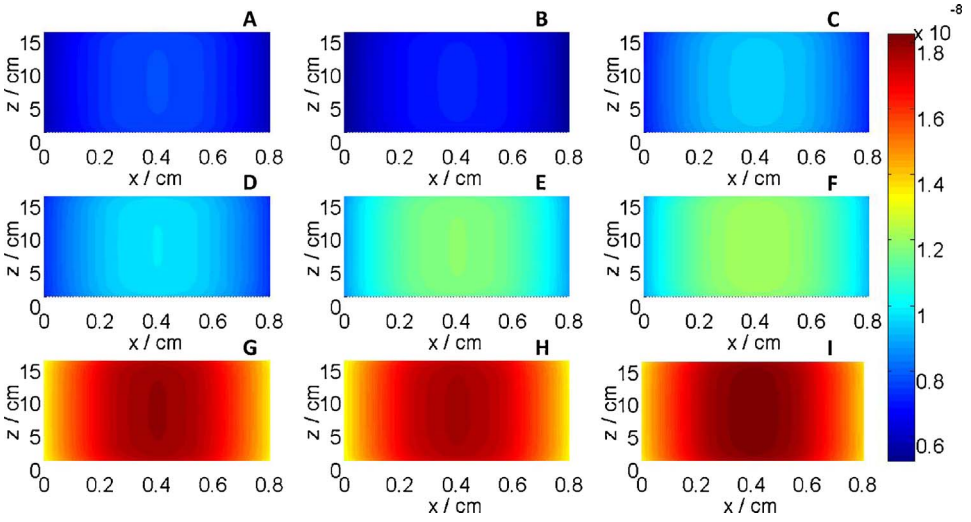

Fig. 9. Local superficial rate of photon absorption (Einstein $cm^{-2} s^{-1}$) of the samples under sunlight-type illumination. (A) TiO_2, (B) $0.005SnTiO_2$, (C) $0.01SnTiO_2$, (D) $0.03SnTiO_2$, (E) $0.05SnTiO_2$, (F) $0.1SnTiO_2$, (G) $0.3SnTiO_2$, (H) $0.5SnTiO_2$, (I) $1SnTiO_2$.

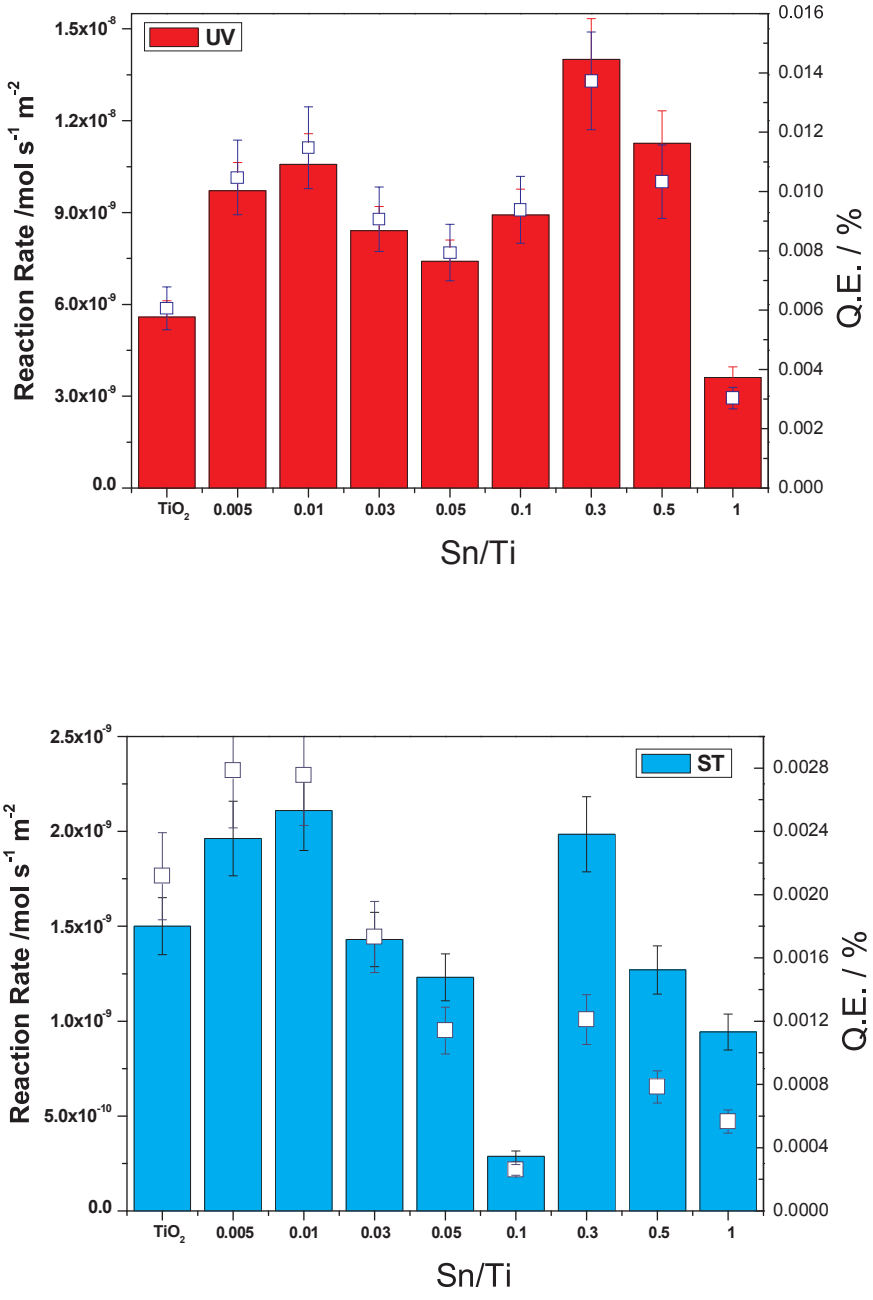

Fig. 10. Reaction rate (bars) and quantum efficiency (squares) obtained for the samples under UV and sunlight-type (ST) illumination.

Table 3
Ratio between catalytic observables of the samples proving maximum activity with anatase and rutile structures ($0.01SnTiO_2/0.3SnTiO_2$ ratio).

Illumination	Reaction Rate Ratio	Quantum Efficiency Ratio
UV	0.76	0.84
Sunlight-type	1.06	2.27

Average Standard Error: 10.5% (Reaction rate) and 18% (Quantum Efficiency).

high activity for both anatase and rutile type samples. The presence of chlorine at surface may have a role in photoactivity. Positive and negative effects has been discussed in the literature depending of a number of experimental variables including the surface and bulk position of the anion, quantity, chemical nature of pollutant and others [2,56–58]. In the Supporting information section we present the quantum efficiency ratio obtained for (selected) samples subjected or not to a rinse treatment to eliminate chloride. Although chloride has an effect in the efficiency, it does not modify its behavior through the series of samples. Specifically, it makes the rutile maximum (sample $0.30SnTiO_2$) slightly more competitive (ca. 15%) with respect to the anatase maximum (sample $0.01SnTiO_2$).

From Scheme 1 and in agreement with previous reports [19,22,54], the main role of surface Sn-containing entities would be the electron capture, allowing holes (preferentially located at the TiO_2 surface) to have a larger probability to reach the pollutant molecule. This happens by different physical (electronic) mechanisms in our anatase and rutile type samples but all of them potentially leading to an enhancement of activity with respect to the bare anatase reference material. More specifically, for anatase the higher position of the Sn-related unoccupied levels (characteristic of size-limited species) favor hot electron transfer (or more likely location as the anatase-type samples do not develop a surface layer but just Sn-containing entities having rather limited dimension) and oxygen activation (Scheme 1). As well known, the relatively poor performance of titania for activation oxygen is related to the relative O_2^-/O_2 redox potential (ca. −0.05 eV vs. NHE) vs. the position

of the anatase conduction band, typically around −0.1 to + 0.2 eV (confinement, surface and defect properties of nanoparticulated systems affects the band position) (2.59). For rutile the relatively similar (to anatase) conduction band position (around −0.2 to + 0.4 eV vs. NHE in nanoparticulated materials; see Refs. [2,59]) suggests a roughly equal situation in a first though. However the shift of the Fermi edge indicates that the situation is completely different. For $30SnTiO_2$ we detect a rather minute shift (Fig. 5; Table 2) and thus we expect relatively similar electronic effects than those taking place in anatase samples although the available rutile surface (the active surface according to catalytic results, no significant activity detected for our SnO_2 reference) is significantly lower. In contrast with the $30SnTiO_2$ sample, the shift occurring for $50SnTiO_2$ and $100SnTiO_2$ (ca. 0.6–0.8 eV detected for the $1SnTiO_2$ sample) would contribute to the rather limited activity presented for all rutile-type samples having high Sn content. Such decrease of activity would be in fact a combination of the strong limitation of the available titania surface and the absence of positive effects of the SnO_x-TiO_2 contact in reactant activation (a fact graphically depicted in Scheme 1 by the degraded color arrows concerning production of activated oxygen species). Contrarily,the band positions corresponding to the amorphous Sn-containing species present at the rutile surface would favor transfer of holes to the rutile phase (as the band position is likely close to the bottom of the rectangle presented in Scheme 1). However as an overall result, a strong decrease of activity is observed for Sn:Ti ratios well above 0.3:1 (Fig. 10) indicating that above mentioned detrimental effects, mostly related to oxygen activation, control activity in these samples.

On the other hand, it is interesting to point out that the band gap of the main (anatase and rutile) $Ti_{1-x}Sn_xO_y$ phases clearly favors activity under UV for all samples here analyzed (see values at Table 1 or Scheme 1). Nevertheless, we note the important activity (as measured by the true quantum efficiency) achieved for the anatase-type $0.01SnTiO_2$ sample under sunlight-type illumination. Whether this is connected to localized electronic states able to absorb visible photons and related at the $Ti_{1-x}Sn_xO_y$ phases or at the interface with surface Sn-containing entities, or is additionally related to an efficient oxygen adsorption and/or activation by the Sn-related surface chemistry remains to be clarified.

We finally note that our comparison of Sn-containing anatase or rutile samples considers samples having different Sn contents. As mentioned previously, comparison of anatase and rutile phases with similar Sn content can be only achieved using samples with strong differences in crystallinity (due to different calcination treatments) and as a consequence in Sn surface vs. bulk distribution, limiting the potential of such comparison. Our purpose was thus to provide information using a complete series of high surface area materials and study the structural, electronic and chemical effects of Sn incorporation and surface decoration occurring in the two most active photo-catalytic titania matrixes, anatase and rutile. As discussed in previous paragraphs, several variables are of significance in the photo-activity as summarized in Table S3 of the Supporting information section. The study presented indicates that chloride as well as Sn-containing surfaces species are able to modify the activity of the $Ti_{1-x}Sn_xO_2$ anatase or rutile main phases. However, the critical appraisal of all the variables indicates the anatase vs. rutile behavior as well as the trend with Sn content is critically affected by the influence of the physico-chemical properties of the composite systems in oxygen activation (Scheme 1; Table S3).

4. Conclusions

In this work we present a study of the photo-catalytic properties of binary Sn-Ti materials. To this end, we analyzed the performance of both anatase and rutile type powders obtained, respectively, with Sn:Ti atomic ratios below and above 0.1:1. For anatase samples, we found the formation of a $Ti_{1-x}Sn_xO_y$ phase (having in all cases a Sn content about 1/3 of the nominal one) which is decorated at its surface by size-limited Sn-containing entities. For rutile type samples the $Ti_{1-x}Sn_xO_y$ phase (also having 1/3 of the nominal Sn content) is significantly decorated by SnO_x entities. The electronic contact of the $Ti_{1-x}Sn_xO_y$ phase with the Sn-containing entities differs in the case of anatase and rutile type dominated samples as summarized in Scheme 1. A strong electronic interaction between the $Ti_{1-x}Sn_xO_y$ phase and the surface, amorphous Sn-containing entities triggers a significant energy shift in Fermi edge, but this only takes place for samples with Sn:Ti ratios above 0.3:1. In anatase samples, presence of surface small Sn-entities favors oxygen activation. In the case of rutile samples the electronic interaction with SnOx entities is a function of the Sn content of the materials. Such an interaction favors hole transfer to the titania phase but is detrimental for oxygen activation. The Sn:Ti ratio of 0.3:1 is the limit above which detrimental effects dominates the catalytic behavior of rutile samples. Other variables influencing activity such as chlorine presence at surface are important but does not influence the trends observed trough the series and thus the comparison of anatase and rutile based catalysts.

The activity in 2-propanol photo-oxidation was tested and two local maxima found along the sample series. Irrespective to the illumination conditions, the maxima correspond to the same samples ($0.01SnTiO_2$ and $0.3SnTiO_2$) having one a main anatase and the other a main rutile type structure. While they display relatively similar values for the corresponding (surface area normalized) reaction rates, the measurement of the true quantum efficiency indicates that the anatase-based system is in fact a more efficient catalyst. The measurement of the quantum efficiency seems thus an indispensable tool to accurately measure the activity of Sn-Ti binary systems and spot out the best performance.

Acknowledgements

The ICP-CSIC group thanks the CSIC for financial support. Work at Sinaloa University acknowledges the support of the DGIP-UAS with the PROFAPI 2015/011 and PROFAPI 2015/012 projects.

Appendix A. Supplementary data

Supplementary material related to this article can be found, in the online version, at doi:https://doi.org/10.1016/j.apcatb.2018.01.075.

References

[1] N.M.R. Hoffmann, M.R. Hoffmann, S.T. Martin, W. Choi, Chem. Rev. 95 (1995) 69–96.
[2] A. Kubacka, M. Fernández-García, G. Colón, Chem. Rev. 112 (2012) 1555–1614.
[3] Y. Ma, X. Wang, Y. Jia, X. Chen, H. Han, C. Li, Chem. Rev. 114 (2014) 9987–10043.
[4] J.C. Colmenares, R. Luque, Chem. Soc. Rev. 43 (2014) 765–778.
[5] X. Li, J. Yu, J. Low, Y. Fang, J. Xiao, X. Chen, J. Mater. Chem. A 3 (2015) 2485–2534.
[6] M. Anpo, M. Takeuchi, J. Catal. 216 (2003) 505–516.
[7] A. Kubacka, M. Fernández-García, G. Colón, J. Catal. 254 (2008) 272–281.
[8] A. Kubacka, G. Colón, M. Fernández-García, Catal. Today 143 (2009) 286–292.
[9] U.G. Akpan, B.H. Hameed, Appl. Catal. A 375 (2010) 1–11.
[10] M. Khan, Y. Song, N. Chen, W. Cao, Mater. Chem. Phys. 142 (2013) 148–153.
[11] H. Feng, M.-H. Zhang, L.E. Yu, Appl. Catal. A 413–414 (2012) 238–244.
[12] J. Liquiang, F. Honggang, W. Baiqi, W. Dejun, X. Baifu, L. Shudan, S. Jiazhiong, Appl. Catal. B: Environ. 62 (2006) 282–291.
[13] Y. Zhao, J. Liu, L. Shi, S. Yuan, J. Fang, Z. Wang, M. Zhang, Appl. Catal. B 100 (2010) 68–76.
[14] Y. Zhao, J. Liu, L.S. Li, S. Yuan, J. Fang, Z. Wang, M. Zhang, Appl. Catal. B 103 (2011) 436–443.
[15] F.E. Oropeza, B. Davies, R.G. Palgrave, R.G. Egdell, PCCP 13 (2011) 7881–7891.
[16] V.B.R. Boppara, R. Lobo, J. Catal. 281 (2011) 156–168.
[17] G.A. Sundaram, M. Yang, K. Nomura, S. Maniarusu, G. Veerappan, T. Liu, J. Wang, J. Phys. Chem. C 121 (2017) 6662–6673.
[18] J. Lin, J. Yu, D. Lo, S.K. Lam, J. Catal. 183 (1999) 368–372.
[19] J. Shang, W. Yao, Y. Zhu, N. Wu, Appl. Catal. A 257 (2004) 25–32.
[20] F. Fresno, C. Guillard, J.M. Coronado, J.-M. Chovelon, D. Tudela, J. Soria, J.-M. Herrmann, J. Photochem. Photobiol. A 173 (2005) 13–21.
[21] F. Fresno, J.M. Coronado, D. Tudela, J. Soria, Appl. Catal. B 55 (2005) 159–167.
[22] F. Fresno, D. Tudela, J.M. Coronado, M. Fernández-García, A.B. Hungría, J. Soria, Phys. Chem. Chem. Phys. 8 (2006) 2421–2430.
[23] H. Luo, T. Takata, Y. Lee, J. Zhao, K. Domen, Y. Yan, Chem. Mater. 16 (2004)

846–849.
[24] R. Sasikala, A. Shirole, V. Sudarsan, T. Sakuntala, C. Sudakar, R. Naik, S.R. Bharadwaj, Int. J. Hydrogen Energy 34 (2009) 3621–3630.
[25] S.K. Sahoo, S. Nigam, P. Sarkar, C. Majumder, Chem. Phys. Lett. 633 (2015) 175–180.
[26] H. Zhuang, Y. Zhang, Z.- Chu, J. Long, X. An, H. Zhang, H. Lin, Z. Zhang, X. Wang, PCCP 18 (2016) 9639–9644.
[27] D. Guerrero-Araque, D. Ramírez-Ortega, L. Lartundo-Rojas, R. Gómez, J. Chem, Technol. Biotechnol. 92 (2017) 1531–1539.
[28] M.H. Harunsani, F.E. Oropeza, R.G. Palgrave, R.G. Egdell, Chem. Mater. 22 (2010) 1551–1561.
[29] R. Long, Y. Dai, B. Huang, J. Phys. Chem. C 113 (2008) 650–657.
[30] F.R. Sensato, R. Custodio, E. Longo, A. Beltrán, J. Andrés, Catal. Today 85 (2003) 145–154.
[31] M.J. Muñoz-Batista, A. Kubacka, A.B. Hungría, M. Fernández-García, J. Catal. 330 (2015) 154–166.
[32] A. Le Bail, H. Duroy, J.L. Forquet, Mater. Res. Bull. 23 (1988) 447–455.
[33] G.K. Williamson, W.H. Hall, Acta Metall. 1 (1953) 22–31.
[34] P. Kubelka, J. Opt. Soc. Am. 38 (1948) 448–457.
[35] M. Fernández-García, A. Martínez-Arias, J.C. Hanson, J.A. Rodriguez, Chem. Rev. 104 (2004) 4063–4105.
[36] L. Palmisano, V. Augugliaro, R. Campostrini, M. Schiavello, J. Catal. 143 (1993) 149–154.
[37] R.J. Brandi, M.A. Citroni, O.M. Alfano, A.E. Cassano, Chem. Eng. Sci. 58 (2003) 979–985.
[38] B. Ohtani, Chem. Lett. 37 (2008) 216–229.
[39] S.E. Braslavsky, A.M. Braun, A.E. Cassano, A.V. Emeline, M.I. Litter, L. Palmisano, V.N. Parmon, N. Serpone, Pure Appl. Chem. 83 (2011) 931–1014.
[40] Y. Cao, T. He, L. Zhao, E. Wang, W. Wang, Y. Cao, J. Phys. Chem. C 113 (2009) 18121–18124.
[41] M.M. Oliveira, D.C. Schnitzler, A.J.G. Zarbin, Chem. Mater. 15 (2003) 1903–1909.
[42] R.D. Shanon, Acta Crystallogr. A 32 (1976) 751–763.
[43] M. Fernández-García, A. Martínez-Arias, A. Fuerte, J.C. Conesa, J. Phys. Chem. B 109 (2005) 6075–6083.
[44] W. Li, A.I. Frenkel, J.C. Woicik, C. Ni, S.I. Shah, Phys. Rev. B 72 (2005) 155315.
[45] Q. Jin, M. Fujushima, M. Nolan, A. Iwaszuk, H. Tada, J. Phys. Chem. C 116 (2012) 12621–12626.
[46] C.D. Wagner, W.M. Riggs, L.E. Davis, J.F. Moulder, G.E. Muilenber (Ed.), Handbook of X-Ray Photoemission Spectra, Perkin-Elmer, Minnesota, 1976.
[47] W.-K.- Jo, K.-H.- Park, Chemosphere 57 (2004) 555–565.
[48] D. Kutzias, Exp. Toxicool. Pathol. 57 (2005) 5–7.
[49] U.B. Celebi, N. Vardan, Atmos. Environ. 423 (2008) 5685–5695.
[50] J. Gunschera, J.R. Anderson, N. Schulz, T. Salthanimer, Chemosphere 75 (2009) 476–482.
[51] S.A. Larson, J.A. Widegren, J.L. Falconer, J. Catal. 157 (1995) 611–625.
[52] A. Wisthaler, P. Strou-Fejsen, L. Fang, A. Hensel, T.D. Mark, D.P. Wyon, Environ. Sci. Technol. 41 (2006) 229–234.
[53] D. Vilduza, R. Portela, C. Ferronato, J.M. Chovelon, Appl. Catal. B 107 (2011) 347–354.
[54] S.Y. Chai, Y.S. Kim, W.I. Lee, J. Electroceram. 17 (2006) 323–326.
[55] M.J. Muñoz-Batista, U. Caudillo-Flores, F. Ung-Medina, M.C. Chávez-Parga, J.A. Cortés, A. Kubacka, M. Fernández-García, Appl. Catal. B 201 (2017) 400–410.
[56] J.G. Li, M. Ikeda, C. Tang, Y. Moriyoshi, H. Hamanka, T. Ishigaki, J. Phys. Chem. 111 (2007) 18018–18024.
[57] R. Yuan, T. Chen, E. Fei, J. Lin, Y. Fu, P. Liu, L. Wu, X. Wang, ACS Catal. 1 (2011) 200–206.
[58] M.J. Torralvo, J. Sanz, J. Soria, G. Garlisi, G. Palmisano, S. Celinkaya, S. Yurdakal, V. Augugliaro, Appl. Catal. B 221 (2018) 140–151.
[59] Y. Zheng, J. Liu, J. Liang, M. Jaroniec, S.Z. Qiao, Energy Environ. Sci. 5 (2012) 6717–6731.